Primary and Secondary Crystallization in a Homogeneous Ethylene-1-Octene Copolymer: Crystallinity Heterogeneity Studied by SAXS

B. Goderis,*,† H. Reynaers,† and M. H. J. Koch‡

Laboratorium voor Macromoleculaire Structuurchemie, Departement Scheikunde, Katholieke Universiteit Leuven, Celestijnenlaan 200F, B-3001 Heverlee, Belgium; and European Molecular Biology Laboratory, EMBL c/o DESY, Notkestrasse 85, D-22603 Hamburg, Germany

Received October 8, 2001; Revised Manuscript Received April 23, 2002

ABSTRACT: The structural changes occurring in a 5.2 mol % 1-octene homogeneous ethylene-1-octene copolymer sample during a cooling and heating cycle at 10 °C/min are described in detail using DSC, AFM, SALLS, and synchrotron WAXD and SAXS. The DSC cooling curve exhibits two exothermic maxima where the high-temperature maximum marks out the temperature window associated with primary crystallization (spherulite nucleation and growth). The morphology after spherulite impingement is characterized by local differences in crystallinity. Secondary crystallization by lamellar insertion is fastest in the largest amorphous areas and results in a spatial homogenization of the crystallinity at a given temperature between the two DSC maxima. The small low-temperature DSC peak is associated with the nucleation of small or imperfect crystals in the confined spaces between existing crystals. During heating, regions with different degrees of crystallinity develop again. An evaluation method for SAXS linear correlation functions is introduced to handle crystallinity heterogeneity. The underlying, basic model is a pseudo-two-phase structure with part of the crystalline−amorphous interphase contributing to the WAXD and DSC crystallinity.

1. Introduction

In the 1990s homogeneous copolymers of ethylene and α-olefins became available on a large scale due to the industrial implementation of metallocene catalysts. Hexyl branches are appended to the linear polyethylene (PE) chain if 1-octene is used as a comonomer. Such fairly bulky aliphatic branches cannot be incorporated in an orthorhombic PE crystal,[1−4] and consequently, crystallinity decreases with increasing amount of 1-octene.

In the thermodynamic model of Flory, the degree of crystallinity at a given temperature is fully determined by the crystallizable ethylene sequence length distribution (ESLD).[5] Sequences that do not have the minimum length required for crystallization at a given temperature, do not crystallize although they can do so at a lower temperature. All sequences of the same length are supposed to merge into extended-sequence crystallites of a related thickness with infinite lateral dimension. Such a thorough selection and segregation of ethylene sequences is, however, never reached and crystallinity is always considerably lower than predicted because of a number of restrictions.

First, *nucleation*, which is a statistical process, takes time and consequently reduces the crystallinity evaluated after finite times. This effect is particularly noticeable at the highest temperatures where nucleation of extended sequence crystals is extremely slow. Upon cooling at a given rate, not-yet-crystallized very long ethylene sequences readily fold and crystallize into lamellar crystals at lower temperatures. At these lower temperatures, shorter ethylene sequences cocrystallize with the folded longer ones provided they have the required minimum length.

Second, besides a minimum length for crystallization at a given temperature a minimum amount of refolding chains is needed for growth into a lamellar habit. At least 60% of the stems reaching the surface of a PE crystal have to bend back into the crystal of origin to avoid the creation of an amorphous phase with too high a density.[6] This problem is known as "*overcrowding*" and in the present case is acute because chain parts with hexyl branches are expelled from the crystal. For this reason, a fraction of the ethylene sequences, which have the critical length for nucleation at a given temperature, do not nucleate and the expected crystallinity is not reached. In principle, such sequences may cocrystallize with shorter ones at lower temperatures, but when the remaining melt is considerably enriched with shorter ethylene sequences, segregation is no longer efficient. Overcrowding is then prevented by the genesis of lamellar crystals with corrugated surfaces or crystals with limited lateral dimensions, including blocklike entities and fringed micelles.

Third, the mobility of free ethylene sequences in the amorphous phase—needed for selection and segregation—is reduced as soon as other sequences that are connected to the same chain are incorporated into crystals. This "*pinning*" gains importance as crystallinity increases. Alizadeh et al.[7] put forward the idea that classical laterally extended lamellar crystals can only be formed when such constraints are minimum as e.g. during primary crystallization. Beyond a given crystallinity, only local segmental motions are possible giving rise to fringed micelle or chaincluster crystals. Blocks can be formed at an intermediate degree of pinning.[7]

The restrictions above give rise to kinetically determined morphologies that depart considerably from Flory's ideal picture. Lamellae are formed at the highest

* To whom correspondence should be addressed.
† Katholieke Universiteit Leuven.
‡ European Molecular Biology Laboratory,

10.1021/ma011749c CCC: $22.00
Published on Web 06/11/2002

temperatures followed by blocks and finally clusters or fringed micelles at the lowest temperatures. The fraction of a particular habit depends on the average comonomer content of a sample. With increasing comonomer content, the *basic morphology* changes gradually from a lamellar structure, over a morphology of lamellae with limited lateral dimensions and granular crystals, to an assembly of fringed micellar crystals.[8,9]

These materials very often display an initial, sharp, high-temperature exothermic peak followed by a broader secondary one at lower temperatures during cooling at a given constant rate in a standard differential scanning calorimetry (DSC) experiment.[7−11] The former signal weakens and finally fades away with increasing comonomer content, whereas the low-temperature exothermic peak broadens, grows, and finally extends down to the glass transition temperature at the highest comonomer contents. The high-temperature peak position is influenced by the cooling rate and melting during subsequent heating occurs at a higher temperature than the previous crystallization peak temperature. Part of the low-temperature exothermic peak displays no cooling rate dependence and no temperature hysteresis upon melting. In the corresponding temperature window, melting and crystallization are essentially reversible. The transition between nonreversible and reversible crystallization is gradual. The position and size of the DSC crystallization and melting peaks is—according to classical views—to a large extent determined by the ESLD[5] (see above), the molar mass distribution and the cooling and heating rates.[10] The ESLD of homogeneous copolymers is, however, unimodal and can consequently not explain multiple crystallization behavior. As an alternative, the high-temperature exothermic peak has been related to classical, nucleation-controlled chain-folded lamellar growth from an unconstrained, nonpinned melt and the low-temperature one to the formation of very small crystallites, including blocklike entities and fringed micelles, from a constrained melt in the confined amorphous nanophases between the already existing crystals.[7,12−14] After the high-temperature peak is passed, the sample's crystallinity may, however, be too low (<10%) to give rise to nanoconfinement and pinning.[15]

In the present article, the crystallization of a vanadium-catalyst-based homogeneous ethylene copolymer with 5.2 mol % 1-octene is discussed. Such copolymers are similar to the more widely spread metallocene-based products and have been the subject of considerable research in the 1980s.[16−19] The chain microstructure and thermal behavior of metallocene-based copolymers do not differ significantly from those of vanadium-based specimens provided that comonomer type and content are comparable.[9,20] However, some metallocene copolymers may contain long chain branches that are usually absent in vanadium-based polymers. The statistics of vanadium-based ethylene−propylene and ethylene−octene copolymers are in between alternating and random.[9,20] The morphology at room temperature[21] and the structural changes after annealing[22] and during continuous heating[23,24] of this particular sample have been reported previously.

Below, the morphological changes during cooling at 10 °C/min are described on different length scales. Emphasis is on compatibility with the structural models used to interpret the small-angle X-ray scattering (SAXS) data, introduced in the Experimental Section. Time-resolved small-angle laser light scattering (SALLS), wide-angle X-ray diffraction (WAXD) and thermal behavior observed by DSC are involved as well. Atomic force microscopy is used to explore the morphology at room temperature and to verify the structural models. Special attention goes to what will be referred to as "secondary crystallization", which is crystallization after the growth front, inside the spherulites, mostly after their mutual impingement, but also during their growth.[25] This involves lamellar insertion in the nanoconfinement between existing crystals as well as the creation of new stacks in large amorphous spherulite inclusions. In principle, crystal thickening and crystal defect elimination also contribute to secondary crystallization, but those are less relevant in the present case. "Primary crystallization" is used to indicate spherulite build up until impingement and involves primary crystals that are active at the spherulite growth front. The influence of the different crystallization steps on subsequent melting behavior is discussed as well.

2. Experimental Section

2.1. Material and Temperature Program. The vanadium-catalyst-based[16] ethylene-1-octene copolymer (DSM code: JW1120)[21] contains 5.2 mol % 1-octene, has a molar mass (M_w) of 30 800 g/mol and a polydispersity (M_w/M_n) of 2. Samples were cooled at 10 °C per min, after a stay of 5 min at 150 °C, to a lowest temperature, which for DSC was 20 °C, for SAXS and WAXD 30 °C, and for SALLS 40 °C. After 2 min the sample was heated to 150 °C at the same rate.

2.2. DSC. Specific heat capacity, $C_p(T)$, data were collected using a Perkin-Elmer DSC7, calibrated with the melting point of indium (156.6 °C) and benzophenone (48 °C) for the temperature and with indium for the enthalpy (28.45 J g^{-1}). The block surrounding the measuring unit was thermostated at −30 °C with liquid nitrogen and the unit was flushed with dry nitrogen. The $C_p(T)$-based mass fraction crystallinity as a function of temperature was calculated according to standard procedures.[26,27]

2.3. SALLS. SALLS measurements were made with an apparatus, similar to the one introduced by Tabar et al.[28] The Hv (polarizer and analyzer perpendicular) and Vv (polarizer and analyzer parallel) scattering patterns were recorded with a CCD camera (Photometrix, ATC200L) every 6 s, corresponding to one pattern for each °C in the temperature ramp. The temperature was controlled by a Mettler FP-82HT hot stage.[29] The samples were inserted as thin films of approximately 50 μm, melt pressed between two glass coverslips. Thin films are needed to avoid distortions of the scattering pattern due to multiple scattering.[30] Corrections for transmission, refraction and reflection were not made since absolute intensities[31] are not needed for the qualitative evaluation outlined below. A melt pattern was subtracted as a background and the spherulite diameter was estimated from the angular position of the maximum in the Hv patterns.[29,32] The error on the estimated diameter must be a few micrometers since an accurate determination of this maximum is hampered by the speckled appearance of the patterns. In contrast, the error on the relative total light scattering intensity of each pattern is negligible and was obtained by integrating over both the scattering angle and the azimuthal angle (Q_{Hv} and Q_{Vv} for Hv and Vv experiments, respectively). These integrated intensities can be written as[33,34]

$$Q_{Hv} = C_1\frac{K}{15}\langle\delta^2\rangle = C_1\frac{K}{15}\phi_{sp}(\phi_{csp}\delta^0_{cr}P_2)^2 \quad (1)$$

$$Q_{Vv} = C_2K\left[\phi_{sp}(1-\phi_{sp})(\overline{\alpha_{sp}}-\alpha_o)(\alpha_t-\alpha_o)+\langle\delta^2\rangle\left(\frac{1}{5}-\frac{\phi_{sp}}{9}\right)\right] \quad (2)$$

where C_1 and C_2 are factors accounting for the fact that the measured intensities are not absolute. The ratio C_2/C_1 is

temperature independent and constant provided the sample transmission change in the Hv experiment is identical to that of the corresponding Vv experiment. To a good approximation, this is the case here since the same sample was used for both subsequent experiments and the same spot was irradiated. K is a calculable constant,[33] ϕ_{sp} is the volume fraction of spherulites, ϕ_{csp} is the volume fraction crystallinity in a spherulite, δ^0_{cr} is the intrinsic anisotropy of a pure crystal, P_2 is a Hermans-type orientation function describing the orientation of the crystals with respect to the spherulite radius, $\overline{\alpha_{sp}}$ is the average polarizability of the spherulite, α_o the polarizability of the matrix surrounding the spherulite, and α_t the tangential polarizability of the spherulite. The form birefringence and the birefringence of amorphous material are neglected in eq 1 and the geometrical correction factors $\cos^2\rho_1$ and $\sin^2\rho_1$ that are present in the original version of eq 2[33] are set equal to 1 and 0, respectively. This simplification is legitimate for scattering angles below 6°, i.e., for spherulite diameters not much smaller than 10 μm. For space filling spherulites, $\phi_{sp} = 1$ and Q_{Vv} is proportional to Q_{Hv} according to

$$Q_{Vv} = \frac{4C_2}{3C_1} Q_{Hv} \tag{3}$$

Finally, Q_{Vv} and Q_{Hv} were normalized to their value at 40 °C. ϕ_{sp} equals 1 at that temperature, as deduced from the characteristic 2-fold symmetry in the Vv-scattering pattern (Figure 7).[32] Consequently, and because of eqs 1−3, all values of $\{Q_{Vv}\}/\{Q_{Vv}^{(40°C)}\}$ are identical to those of $\{Q_{Hv}\}/\{Q_{Hv}^{(40°C)}\}$ at temperatures where ϕ_{sp} equals 1 and $\{Q_{Vv}\}/\{Q_{Vv}^{(40°C)}\}$ is larger than $\{Q_{Hv}\}/\{Q_{Hv}^{(40°C)}\}$ at temperatures where ϕ_{sp} is smaller than 1.[29]

2.4. AFM. Atomic force microscopy experiments were performed with a Nanoscope III scanning probe microscope equipped with a J-scanner. AFM images were obtained under ambient conditions while operating the instrument in the tapping mode and using a silicon low frequency tapping tip (NCL type from Nanosensors, Wetzlar, Germany). Height and phase images were recorded simultaneously in the light tapping regime[35,36] to emphasize topographic features in the phase image. A frequency slightly below the fundamental resonance frequency of the cantilever (typically 170 kHz) was selected. The set point was chosen at 90% of the free amplitude oscillation (free cantilever oscillation: 65 nm peak-to-peak). Images are matrices of 512 × 512 data points and were recorded with typical scan speeds of 1 line/s. Samples were first compression molded between a glass slide and a silicon wafer. The wafer was removed at room temperature and the samples were reheated to 200 °C and cooled after 5 min at 10 °C/min in a Mettler FP-82HT under nitrogen atmosphere. The free surface was examined at room temperature without any further treatment.

2.5. Synchrotron SAXS and WAXD. Time-resolved SAXS and WAXD data were collected simultaneously every 12 s during the temperature program, which corresponds to one pattern per 2 °C. The ×33 double focusing camera of the EMBL in HASYLAB was used on the storage ring DORIS of the Deutsches Elektronen Synchrotron (DESY), Hamburg, Germany, at a wavelength of 1.5 Å.[37] A standard data acquisition system was used.[38,39] The 1 mm thick samples were sealed between 15 μm thick aluminum foils,[40] and the temperature was controlled by a Mettler FP-82HT hot stage, flushed with cooled air to achieve the required cooling rate. The WAXD and SAXS intensities were normalized to the intensity of the primary X-ray beam and the SAXS patterns were additionally corrected for the detector response. The scattering vector axis of the SAXS region was calibrated using the first nine orders of dry calcified collagen, and the 110 and 200 reflections of a quenched linear polyethylene were used to calibrate the WAXD axis.[22]

A linear background was subtracted from the WAXD data, which were collected over the angular range $11.7 \le 2\theta \le 46°$ (with 2θ the scattering angle). The remaining pattern was fitted using three Gaussians for the amorphous halo, the 110 reflection, and the 200 reflection, respectively. The integrated intensity of the 110 reflection was taken as a WAXD crystallinity index. The crystalline density was calculated from the angular positions of the Gaussian's maxima through the 110 and 200 reflections and assuming the length of the orthorhombic unit cell in the c direction (the molecular chain direction) to be constant at 2.547 Å. No density data are available for crystallinities below 15% because no precise peak positions could be assigned to the observed weak reflections.

An averaged melt pattern was subtracted as a background from the SAXS patterns, collected over the angular range $0.0015 \le s \le 0.032$ Å^{-1} (with $s = 2 \sin\theta/\lambda$, 2θ the scattering angle, and λ the wavelength). The data in the range $0.011 \le s \le 0.032$ Å^{-1} were fitted with eq 4,[41] substituted by the fitting results and extrapolated to $s = 0.09$ Å^{-1} after subtracting the background B as described earlier:[29]

$$B + \frac{P}{s^4} \exp(-4\pi^2\sigma^2 s^2) \tag{4}$$

In eq 4, P represents the Porod constant.[42] The variable σ is related to the transition layer with a thickness equal to 3σ. After an appropriate extrapolation to zero angle,[29] $I(s)$ was obtained and linear correlation functions, $K(x)$, were calculated by cosine transformation:

$$K(x) = \int_0^\infty I(s) s^2 \cos(2\pi x s)\, \mathrm{d}s \tag{5}$$

The value of $K(0)$ equals the total scattering power or invariant due to the actual pseudo two-phase structure, i.e., the structure with transition layers between the two phases. The (relative) invariant or total scattering power of the corresponding ideal two-phase structure, Q_{id}, is obtained from the intercept of the linear regression to the autocorrelation triangle.[43] In principle, the autocorrelation triangle displays a linear part in the case of laterally extended lamellar systems and as long as the crystalline lamellar core is thicker than the interphase. In that case, the SAXS data can be processed to yield the parameters that describe the corresponding ideal two-phase system[29,43] characterized by the reference state densities and a sharp crystalline−amorphous interface in the middle of the original interphase.[29,44]

The largest uncertainty in the present SAXS data processing is found in the fitting and extrapolation with eq 4. The associated errors essentially propagate in deviations from linearity in the autocorrelation triangle of $K(x)$ whereas the remaining part of $K(x)$ is not affected.[29] In the present case, these deviations are considered not to be due to departures from the structural model since AFM proves the opposite. Furthermore, they are statistical rather than systematic. Standard errors that are proportional to this deviation from linearity were determined[45] in a least squares linear regression for both the slope and the intercept (Q_{id}) and propagated during further processing according to the procedures discussed in section 2.7. Error bars are added to the data when appropriate and in particular to make clear that a distinction between the different SAXS models is legitimate. The long period, which is extracted from the position of the first side maximum in $K(x)$, is considered to be without error.

2.6. Structural Models for the Analysis of *K*(*x*). A new procedure is introduced in the next paragraph to analyze SAXS linear correlation functions of morphologies that consist of two fractions with a different degree of crystallinity, referred to as the "CA−CA model". It is an extension of the classical procedure for systems that resemble the "A−CA model", in which the presence of semicrystalline regions in an amorphous matrix is assumed.[29] In both models, the semicrystalline regions consist of isotropically oriented one-dimensional stacks of alternating crystalline and amorphous layers. Both processing procedures can in principle also deal with assemblies of isotropically oriented, isolated crystalline lamellae in an amorphous matrix and with samples that are completely filled with one-dimensional lamellar stacks that have the same crystalline and amorphous layer thickness distributions and

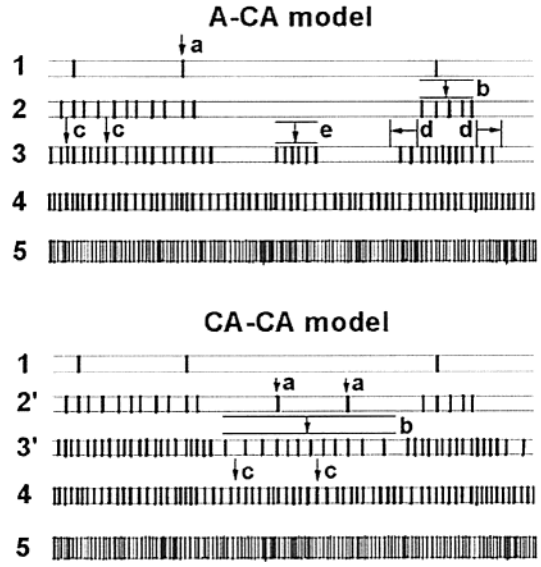

Figure 1. Comparison of the structural evolution assumed in the A−CA and CA−CA models. Steps in the morphology development are numbered whereas the processes involved are labeled with letters. The thin vertical black lines represent edge-on lamellar crystals that are generated in a horizontal one-dimensional stack.

stack organization. Both procedures can thus be used to follow the transformation of an amorphous melt into a homogeneous semicrystalline morphology. The way in which this is envisaged, however, depends on the model as schematically illustrated in Figure 1.

In the A−CA model isolated lamellae may form first according to process a, leading to step 1, and transform according to process b into an assembly of stacks, i.e., step 2. In going from step 2 to step 3, the crystallinity increases by lamellar insertion (process c), stack thickening (process d), and the formation of new stacks (process e). Finally space is completely filled with stacks in step 4. The crystallinity may further increase by ongoing lamellar insertion leading to step 5. The SAXS analysis according to this model cannot distinguish between processes e and d and the stacks that are formed in process e are assumed to have the same crystallinity and stack build up as those that were generated earlier by the sequence a−b−c. It is also taken for granted that stacks thicken with a crystallinity equal to the instantaneous crystallinity in the center of the stack, although this central crystallinity may have been accomplished at earlier times along a more gradual route, i.e., along processes a, b, and c. In fact, at each time all stacks are assumed to be identical.[43] This differs from the CA−CA model in which new stacks are allowed to grow from isolated lamellae, generated between earlier formed stacks as depicted in Figure 1 (step 2′). Intermediate stages with fractions that have a different crystallinity are possible too as, e.g., in step 3′. At each stage, however, only *two* different fractions are allowed.

2.7. Model-Dependent SAXS Correlation Function Analysis. For both the A−CA and CA−CA models, the basic model is a two-phase crystalline−amorphous one. In principle, Q_{id} does not depend on how the crystallinity is distributed over the sample volume and is a simple function of the total crystallinity, Φ

$$Q_{id} = C\Phi(1 - \Phi)(d_c - d_a)^2 \quad (6)$$

with C a temperature independent constant and d_c and d_a the temperature-dependent mass densities of the crystalline and amorphous phases, respectively. Theoretically, electron densities should be used in eq 6, but as only PE is present, it is correct to write mass densities provided that a scaling factor is included in the constant C.

For systems with regions of two different crystallinities

$$\Phi = \alpha_1\phi_1 + \alpha_2\phi_2 \quad (7)$$

with α_1 and α_2 the respective volume fractions and ϕ_1 and ϕ_2 the corresponding internal crystallinities and of course

$$\alpha_1 + \alpha_2 = 1 \quad (8)$$

A combination of eqs 6 and 7 yields

$$Q_{id} = C\{\alpha_1\phi_1(1 - \phi_1)(d_c - d_a)^2 + \alpha_2\phi_2(1 - \phi_2)(d_c - d_a)^2 + \alpha_1\alpha_2(d_1 - d_2)^2\} \quad (9)$$

with

$$d_1 = \phi_1 d_c + (1 - \phi_1)d_a \quad (10)$$

the average density in the fraction with an internal crystallinity ϕ_1 and

$$d_2 = \phi_2 d_c + (1 - \phi_2)d_a \quad (11)$$

the average density in the fraction with an internal crystallinity ϕ_2. The first two terms in eq 9 represent the scattering originating from each of the two fractions scattering independently with a scattering contribution proportional to their volume fraction. The third term represents the contribution of a supermorphology characterized by the two fractions and a contrast given by their difference in internal (electron) density. In general, this supermorphology has no particular order and consequently contributes scattering that decays exponentially toward large angles.[46] This decay will be faster if in addition the interfaces between the two fractions are not infinitely sharp.[41] If large-scale (micrometer) dimensions are involved, this third term will only contribute to the intensity at very low angles, which are in practice not accessible. Light scattering can probably be observed if the characteristic distance is larger than approximately 1 μm. In that case, the total observed scattering power can be considered as a superposition of the volume fraction weighted contributions of the two fractions only:

$$Q_{id} = C\{\alpha_1\phi_1(1 - \phi_1)(d_c - d_a)^2 + \alpha_2\phi_2(1 - \phi_2)(d_c - d_a)^2\} \quad (12)$$

If, e.g., ϕ_2 equals zero, eq 12 reduces to eq 13, which describes Q_{id} for an A−CA system:

$$Q_{id} = C\alpha_S\phi_L(1 - \phi_L)(d_c - d_a)^2 \quad (13)$$

To distinguish between the two models α_1, the volume fraction of semicrystalline regions, is replaced by α_S and ϕ_1, the local crystallinity in the semicrystalline regions, by ϕ_L.

The scattering profile of a CA−CA system equals the volume fraction weighed superposition of the two fraction-characteristic scattering profiles. Consequently, $K(x)$ of a CA−CA scattering pattern is equal to the volume fraction weighed sum of the $K(x)$ functions calculated from the two respective scattering patterns. On this account, the linear regression to the autocorrelation triangle of $K(x)$ can be written as

$$y = C(d_c - d_a)^2\left\{\alpha_1\left[-\frac{O_{S1}}{2}x + \phi_1(1 - \phi_1)\right] + \alpha_2\left[-\frac{O_{S2}}{2}x + \phi_2(1 - \phi_2)\right]\right\} \quad (14)$$

based on the equation given previously for the linear regression to the autocorrelation triangle of a homogeneous two-phase crystalline−amorphous system.[29] In eq 14, O_{S1} and O_{S2} are the surface-to-volume ratios in fractions 1 and 2. The solution of eq 14 for $y = 0$ yields

$$x = A = \frac{\alpha_1\phi_1(1-\phi_1) + \alpha_2\phi_2(1-\phi_2)}{\alpha_1 O_{S1}/2 + \alpha_2 O_{S2}/2} \quad (15)$$

where A represents the intersection of the linear regression to the autocorrelation triangle with the abscissa. The denominator of this equation can also be written as $O_S/2$, with O_S the overall surface-to-volume ratio. Equation 16 is the equivalent of eq 15 for the A−CA model[29]

$$A = \phi_L(1-\phi_L)\frac{2}{O_{SL}} = \phi_L(1-\phi_L)\mathrm{LP} \quad (16)$$

and is obtained by setting ϕ_2 and $O_{S2}/2$ equal to zero as appropriate for an amorphous fraction. In addition, $O_{S1}/2$ has been renamed to $O_{SL}/2$ just like ϕ_1 has been to ϕ_L Equation 16 is sometimes referred to as the quadratic expression[29] and can be used to calculate ϕ_L. LP, the number-average long period associated with the semicrystalline fraction, can replace $2/O_{SL}$ if the lamellar side surfaces do not contribute significantly to O_{SL}. This is legitimate for laterally extended lamellar crystals. Calculation of ϕ_L becomes straightforward if LP can be read from the position of the first side-maximum in $K(x)$ as is the case for symmetric distance distributions.[47,48]

The minimum of the correlation function, $K(x)_{min}$, is described by eq 17 if, in the framework of the CA−CA model, both contributing correlation functions have a plateau minimum in the same x range

$$K(x)_{min} = -C[\alpha_1\phi_1^2 + \alpha_2\phi_2^2](d_c - d_a)^2 \quad (17)$$

again based on the equation for homogeneous two-phase crystalline−amorphous systems.[29,43] A flat $K(x)_{min}$ occurs if both ϕ_1 and ϕ_2 are low (typically below 0.25). After normalization of $K(x)$ with the actual Q_{id} as described by eq 12, CF(x) is obtained[29] with a plateau minimum

$$\mathrm{CF}(x)_{min} = \frac{-[\alpha_1\phi_1^2 + \alpha_2\phi_2^2]}{[\alpha_1\phi_1(1-\phi_1) + \alpha_2\phi_2(1-\phi_2)]} \quad (18)$$

which is reduced to eq 19 for an A−CA system:[29,43]

$$\mathrm{CF}(x)_{min} = -\frac{\phi_L}{1-\phi_L} \quad (19)$$

The latter equation provides an alternative means to calculate ϕ_L. Independent information is needed to decide whether ϕ_L represents the crystalline or the amorphous fraction. This also holds for eq 16, which yields two solutions for ϕ_L. In this paper the minority fraction was considered to be crystalline over the full temperature range, as this proved to be most compatible with the DSC crystallinity values. This also holds for the evaluations based on the CA−CA model.

When values for the temperature-dependent densities are available and if the constant C can also be obtained, one can calculate Q_C, according to

$$Q_C = \frac{Q_{id}}{C(d_c - d_a)^2} \quad (20)$$

In the present case, C was obtained from eq 13 by assuming a homogeneous morphology at temperatures below 50 °C. For such morphologies α_S equals 1 and ϕ_L, which can be obtained from the correlation function according to eq 16, corresponds to the sample's overall crystallinity. Consequently, C is the only remaining unknown in eq 13, since the temperature dependent mass densities of fully crystalline and amorphous PE are available from the literature.[49] The value of C that was actually used throughout is the average of the values in the temperature range below 50 °C.

A combination of eqs 15, 8, 12, and 20 yields an expression for α_1:

$$\alpha_1 = \frac{Q_C/A - O_{S2}/2}{O_{S1}/2 - O_{S2}/2} \quad (21)$$

For morphologies with both fractions resembling laterally extended lamellar stacks $O_{S1}/2$ and $O_{S2}/2$ can be replaced with the corresponding inverse long periods $1/LP_1$ and $1/LP_2$. Obviously, the calculation of α_S is straightforward if $K(x)$ displays two maxima at positions equal to LP_1 and LP_2. Equation 21 reduces to eq 22 for an A−CA system:

$$\alpha = \frac{2Q_C}{AO_{SL}} = \frac{Q_C}{\phi_L(1-\phi_L)} \quad (22)$$

When values for $O_{S1}/2$ and $O_{S2}/2$ are available, one can also calculate ϕ_1 and ϕ_2, provided it can be assumed that the average crystal thickness, T_c, in fraction 1 is equal to that in fraction 2. Accordingly ϕ_1 can be written as

$$\phi_1 = \frac{T_c O_{S1}}{2} \quad (23)$$

and ϕ_2 as

$$\phi_2 = \frac{T_c O_{S2}}{2} \quad (24)$$

By combining eqs 23 and 24 with eqs 8, 12, and 20, an expression for T_c is obtained:

$$T_c = \left\{\left[\frac{\alpha_1 O_{S1}}{2} + \frac{(1-\alpha_1)O_{S2}}{2}\right] + \sqrt{\left(\frac{\alpha_1 O_{S1}}{2} + \frac{(1-\alpha_1)O_{S2}}{2}\right)^2 - 4\left(\frac{\alpha_1 O_{S1}^2}{4} + \frac{(1-\alpha_1)O_{S2}^2}{4}\right)Q_C}\right\} \Big/ 2\left(\frac{\alpha_1 O_{S1}^2}{4} + \frac{(1-\alpha_1)O_{S2}^2}{4}\right) \quad (25)$$

With T_c as input, ϕ_1 and ϕ_2 can be calculated using eqs 23 and 24.

The parameters α_1, α_2, ϕ_1, ϕ_2, and T_c can thus be calculated straightforwardly if $K(x)$ displays two maxima at positions equal to LP_1 and LP_2. Morphologies that potentially give rise to two maxima can be represented by structure 3′ in Figure 1. Very often and also in the present case, no second maximum is observed. This does not necessarily mean that fraction 2 is amorphous and that the A−CA model is applicable. The crystallinity in fraction 2 can be so low that the crystals scatter like isolated lamellae or the stacking order can be so poor that there is no characteristic periodicity, such as, e.g., in structure 2′ of Figure 1. These crystals obviously contribute to the scattering patterns and the correlation functions with a characteristic high value for $2/O_{S2}$, which, unfortunately, is not easily extracted. Furthermore, the actual structure may have a skew crystallinity distribution, rather than a bimodal one. The observed LP in this case resembles a most probable rather than a true number-average value. Application of the CA−CA approach in the latter case is appropriate and discussed in section 2.8.

The absence of a value for $2/O_{S2}$ can be overcome and hence the equations solved if the internal crystallinity in both fractions is low. T_c, which in that case can be obtained along another route, can be used as an alternative input, still assuming that its value is the same in both fractions. At low ϕ_1 and ϕ_2 values, $K(x)$ or CF(x) displays a plateau minimum. By combining eqs 14, 17, 23, and 24, it can be shown that the linear regression to the autocorrelation triangle intersects the horizontal line through $K(x)_{min}$ at $x = T_c$ as in the classical analysis.[29,43] This holds for the A−CA and CA−CA models as well as for multiphase models. Knowing T_c, ϕ_1 can be calcu-

lated by replacing $O_{S1}/2$ with $1/LP_1$ in eq 23. The position of the observed single maximum (LP) is arbitrarily associated with fraction 1 and labeled LP_1. Combining eqs 12, 20, 21, 23, and 24 yields eq 26 to calculate ϕ_2 in which for convenience $O_{S1}/2$ is replaced by $1/LP_1$

$$\phi_2 = \frac{-Y + \sqrt{Y^2 - 4XZ}}{2X} \tag{26}$$

with

$$X = \frac{Q_C}{A} - \frac{1}{LP_1}$$

$$Y = \frac{Q_C - \phi_1(1-\phi_1)}{T_c} + \frac{1}{LP_1} - \frac{Q_C}{A}$$

$$Z = -\frac{Q_C}{LP_1} + \frac{Q_C\phi_1(1-\phi_1)}{A}$$

Finally, α_1 can be calculated by using eq 27, which is a combination of eqs 21 and 24:

$$\alpha_1 = \frac{Q_C/A - \phi_2/T_c}{1/LP_1 - \phi_2/T_c} \tag{27}$$

For the present data, the necessary condition for the use of $K(x)_{min}$ or $CF(x)_{min}$ (i.e., the presence of a plateau minimum) is fulfilled in the temperature regions of interest.

In the framework of the A−CA model, the number-average crystalline lamellar thickness, T_c, was calculated from the product of LP with ϕ_L. In general ϕ_L was obtained from eq 16. Only at the two highest temperatures of the melting experiment T_c was obtained from the intersection of the linear regression to the autocorrelation triangle with $y = K(x)_{min}$ since at these temperatures LP could not be extracted from the very broad maximum in $K(x)$. At these temperatures ϕ_L was obtained from eq 13.

Finally, $\alpha_S\phi_L$ is a measure for the total volume fraction crystallinity, Φ, in the A−CA case,[29] as is $\alpha_1\phi_1 + \alpha_2\phi_2$ for CA−CA systems. Equations to analyze correlation functions of homogeneous morphologies (steps 4 and 5 in Figure 1) are easily obtained by putting α_S equal to 1 in the equations that are appropriate for the A−CA model. Identical results are obtained if ϕ_1 is put equal to ϕ_2 in the CA−CA equations and obviously it holds that $\phi_L = \phi_1 = \phi_2 = \Phi$.

2.8. Extension of the CA−CA Approach to Continuous Crystallinity Distributions. Blundel[47] and later Crist[48] reported that the observed LP is a true number-average value for homogeneous morphologies, i.e., morphologies with identical stacks all over the volume, provided the internal LP distribution is symmetric, e.g., Gaussian. Similarly, in the case of two kinds of stacks with a Gaussian internal LP distribution, two maxima will appear in $K(x)$ that are number-average LP values. Clearly, the CA−CA approach is most suited for the characterization of such morphologies. Considering a higher number of different stacks (fractions) is relevant but unfortunately leads to unsolvable equations. Strobl and Müller first reported the importance of stack (crystallinity) heterogeneity to explain the SAXS patterns of melt crystallized low-density PE.[50] Blundell[47] and Lee[51] did systematic studies on *continuous* crystallinity distributions by means of model scattering profiles. One maximum is observed in $K(x)$ with a value close to the true number-average LP value, also in the case of stacks with an internal Gaussian LP distribution but with the mean LP different between different stacks according to a Gaussian distribution.[47] In this particular case of heterogeneous morphologies, eq 16 with $\alpha_S = 1$ thus yields the correct overall (average) crystallinity values. One can expect two number-average LP maxima in $K(x)$ if the heterogeneous crystallinity distribution is described by two Gaussians. The CA−CA approach in that case will produce two fractions with a crystallinity related to the peak values of the two Gaussians. When the peaks of the Gaussians are not well separated or if they are rather broad or if one of them is much less intense than the other, very likely only one LP will be observed in $K(x)$. Such distributions may be labeled "skew" rather than truly "bimodal" and the single observed long period may well represent a most probable rather than a true number-average value. As discussed in section 2.7, T_c can be used as an alternative input for the missing value of LP_2. In the present case, the CA−CA approach *artificially* divides skew crystallinity spectra in two fractions. One fraction will be assigned a most probable crystallinity and the other a lower or higher crystallinity, depending on which way the distribution is skewed. Qualitatively one can state that a skew crystallinity distribution is divided into two Gaussian distributions, with the peak of one Gaussian at the position of the most probable LP (or crystallinity). It is important to stress that the LP distribution in each separate stack is also assumed to be Gaussian.

Very clearly, introduction of stack heterogeneity gives rise to forward or zero-order scattering of which the largest scattering angle increases with decreasing stack size. Lee et al. recognized that when the zero-order scattering component is not discarded before calculating the correlation function, the latter is *shifted upward* (tails of correlation functions do not approach zero) and *distorted*.[51] In the framework of considerations on the CA−CA model given above, the shift of the correlation function can be understood as follows. In the limiting case of a supermorphology characterized by extremely large distances, the associated scattering tends to a sharp spike at $s = 0$. The Fourier transform of such a function is a horizontal line at a value equal to its integral. In the present case this constant, which is added to the $K(x)$, corresponds to the third term in eq 9: $C\alpha_1\alpha_2(d_1 - d_2)^2$. In practice the characteristic length scale associated with the supermorphology, a, has a finite size and the function that is added is not constant and thus accounts for distortions. This function can be approximated by the linear correlation function, $K(x)$, of random scatterers with a characteristic length a.

$$K(x) = C\alpha_1\alpha_2(d_1 - d_2)^2\left[\exp\left(\frac{-x}{a}\right) - \frac{x}{a}\exp\left(\frac{-x}{a}\right)\right] \tag{28}$$

Equation 28 is based on the corresponding (normalized) exponential 3D correlation function given by Debye et al.,[46] $\gamma(r)$, and the general relationship between $\gamma(r)$ and the corresponding linear correlation functions, $\gamma_1(x)$:[52]

$$\gamma_1(x)_{x=r} = \frac{d\{r\gamma(r)\}}{dr} \tag{29}$$

The factor $C\alpha_1\alpha_2(d_1 - d_2)^2$ in eq 28 accounts for not having normalized the correlation function to the total scattering power.[29] Assuming that the contribution to $K(x)$ due to large scale heterogeneities can be described by eq 28 one can calculate that the deviation from a constant value is less than 10% for $x <$ LP if a is 20 times larger than LP. In most cases, the value of LP for polymers is between 100 and 600 Å implying that a has to be larger than 0.2 or 1.2 μm, respectively. Such distances give rise to X-ray scattering at commonly, inaccessibly low angles but at high a values to excess Vv-light scattering. If a is much smaller or becomes comparable to LP, the fractions with a different crystallinity will no longer scatter independently. Such cases have a characteristic pronounced zero-order scattering inside the experimental window and are best treated as single stack systems with broad layer thickness distributions.[48]

2.9. Babinet's Principle. Problems arise for skew as well as for truly bimodal crystallinity distributions if there is an overlap with the 0.5 crystallinity line because of Babinet's reciprocity theorem, which states that an exchange of the densities in a two-phase structure leaves the scattering function unchanged. In the present copolymer case, both ϕ_1 and ϕ_2 are assumed to be below 0.5 in the CA−CA analysis. The data evaluation is similar if both crystallinities are above 0.5 since the scattering patterns do not change when the

crystalline and amorphous entities are swapped. This holds for the observed part as well as for the zero-order component of the scattering profile, and the crystallinity values simply have to be mirrored with respect to 0.5. If, however, the crystalline and amorphous parts are reversed in only one of the two fractions, then likewise the observed part of the scattering pattern does not change but the contrast (hence the intensity) associated with the zero-order scattering is increased. So, *four* crystallinity values are compatible with the observed part instead of the usual two in the case of two fractions with a different crystallinity and a not-observed zero-order scattering. The number of possibilities of course increases dramatically with the number of different fractions present in the sample.

2.10. Position of the Novel Processing Procedure with Respect to Established Methods. The classical analysis of linear correlation functions for homogeneous morphologies was introduced decades ago by Vonk et al.[53,54] and Strobl et al.[43] Their approaches are identical, provided that the normalization of the correlation function is properly taken into account.[29] The overall crystallinity[29] can be calculated using these methods if α_S is added, according to what is currently labeled as "the A−CA approach". The A−CA model is a limiting case of the CA−CA model with the crystallinity in one of the fractions equal to zero. A zero crystallinity in one of the fractions is generated automatically if correlation functions of A−CA systems are analyzed according to the CA−CA procedures. At all times and erroneously, however, a zero crystallinity in one of the fractions is generated if CA−CA systems are treated with A−CA procedures. In that respect the CA−CA approach has a clear advantage. Although the method is designed in particular for bimodal crystallinity cases it may be useful to characterize skew crystallinity distributions too. In particular since—aside from the tedious comparison of experimental curves with model scattering patterns and correlation functions[47,51]—no SAXS evaluation method has been reported yet to handle such morphologies.

To our knowledge, interface distributions functions,[55] have not yet been studied systematically from the perspective of stack heterogeneity. Recently a combination of correlation and interface distribution function analysis led to the conclusion of coexisting closely packed crystalline−amorphous stacks and low crystalline regions in an amorphous matrix in the case of linear polyethylene during (quasi) isothermal crystallization.[40] The calculation of interface distribution functions, however, requires the elimination of effects from transition layers[55] and readily introduces artificial oscillations due to truncation errors. This appeared to be so in the present copolymer case even after applying smoothing procedures. Consequently interface distribution functions are not included. It is anticipated, however, that overlapping distributions will be very difficult to discriminate and quantitative evaluations thus nearly impossible if no a priory model is assumed for the layer thickness distributions and the local packing in the fractions.

In this paper, the correlation functions are processed according to both the classical A−CA and new CA−CA approaches and discussed while aiming at compatibility with the outcome of other techniques.

3. Results and Discussion

Figure 2 displays the DSC $c_p(T)$ traces and the derived crystallinities, which are in reasonable agreement with the WAXD results of Figure 3. During cooling there is initially a fairly sharp increase of the crystallinity around 90 °C followed by a slower increase toward lower temperatures. Around 50 °C there is a small additional maximum in the $c_p(T)$ cooling curve with an associated steeper increase in the DSC crystallinity. This effect, however, is not observed in the WAXD crystallinity estimate.

The slopes of the copolymer crystalline density data and Swan's reference data for linear polyethylene[49] in Figure 3 are comparable, reflecting thermal expansion.

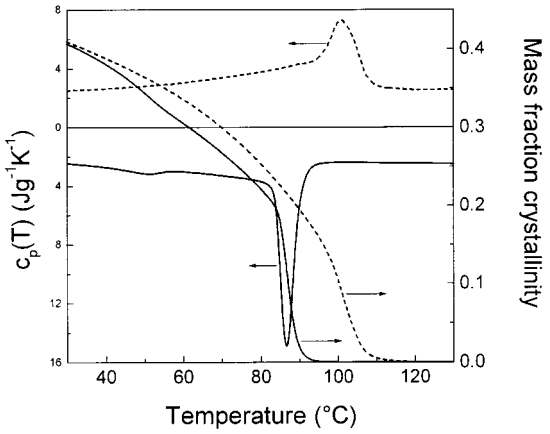

Figure 2. DSC cooling (full line) and heating (dashed line) $c_p(T)$ curves recorded at 10 °C/min, together with the DSC based crystallinity values represented with corresponding line types.

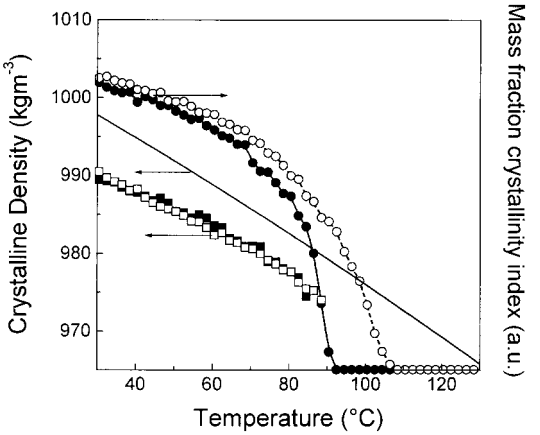

Figure 3. WAXD (mass-based) 110 crystallinity index during cooling (full circles) and heating (open circles) and the respective experimental crystalline densities (cooling, full squares, and heating, open squares). The full line is the reference crystalline density of linear polyethylene by Swan.[26]

The copolymer's density, however, is below Swan's estimates. The crystalline density of ethylene copolymers at a given temperature is known to decrease with increasing overall comonomer content.[19,21] In the case of hexyl side chains, this is thought to be related to a concomitantly decreasing average crystal thickness.[1,56,57] The thinner a crystal, the higher the fraction of crystalline unit cells close to the surface where local stresses and conformational defects give rise to expansion. This set of expanded unit cells can be considered as the onset of the transition layer between crystalline and amorphous material.[58] Fitting with eq 4 actually revealed the presence of a transition layer with a thickness fluctuating around 10 Å. This value agrees with earlier estimates,[21] but it should be remembered that σ tends to be overestimated if a constant background is chosen and if data are collected over a limited angular range.[29] The existence of a transition layer is, however, widely accepted since there are numerous techniques besides SAXS that reveal its presence.[58] In any case, an overestimated σ value does not influence the SAXS crystallinity estimates of the corresponding ideal two-phase structure.[29] In that respect, it is of interest to mention that Swan's amorphous and crystalline densities were used during SAXS data processing and not the available experimental crystalline density data,

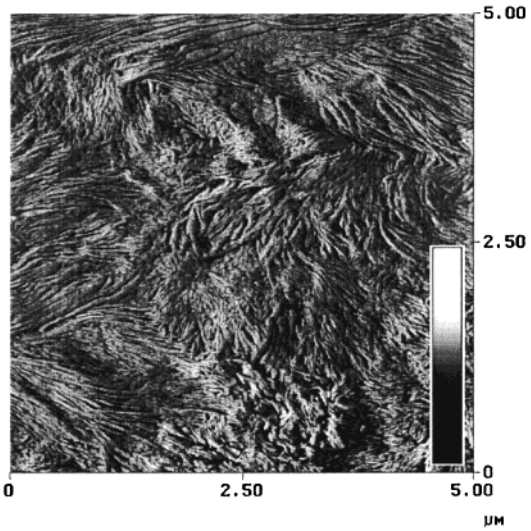

Figure 4. Tapping mode AFM phase image of the morphology at room temperature after cooling at 10 °C/min. The gray scale—indicating the relative phase shift—is delimited at 80 and 0° at the white edge and black edge, respectively.

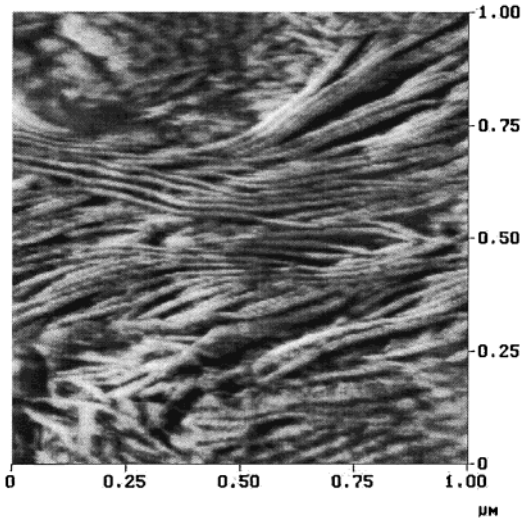

Figure 5. Low scale tapping mode AFM phase image of the morphology at room temperature after cooling at 10 °C/min. The gray scale associated with the relative phase shift is identical to that in Figure 4.

because it yields a better match with the crystallinity estimates of DSC and WAXD. Swan extracted his crystalline densities from highly crystalline PE in which no significant transition layer influences can be expected. This better fit not only implies that the core of the crystallites consist of unexpanded, regular orthorhombic unit cells with a Swan-like reference density but also that at least part of the transition layer is DSC and WAXD crystalline with a contribution to the crystalline peak positions (density) and areas (crystallinity).

The existence of extended lamellar crystallites, which is a requirement for the SAXS processing procedures, is apparent from the AFM phase image in Figure 4. In addition, no large amorphous areas are present at room temperature and the distribution of the crystallites seems to be uniform, justifying the assumption of α_S being equal to 1 at low temperatures. The crystal thickness was estimated from lamellae that were thought to lay essentially edge on as present in the center of Figure 5 and are typically between 50 and 70 Å.

Figure 6 displays $\{Q_{Hv}\}/\{Q_{Hv}^{(40°C)}\}$, $\{Q_{Vv}\}/\{Q_{Vv}^{(40°C)}\}$, and the spherulite diameter as a function of temperature. Although not obvious from this figure, the onset temperatures of the intensity increase in the cooling experiment for $\{Q_{Hv}\}/\{Q_{Hv}^{(40°C)}\}$and $\{Q_{Vv}\}/\{Q_{Vv}^{(40°C)}\}$ are identical (94 °C). This also holds for the end temperature during heating (110 °C). During cooling, $\{Q_{Vv}\}/\{Q_{Vv}^{(40°C)}\}$ is larger than $\{Q_{Hv}\}/\{Q_{Hv}^{(40°C)}\}$between 94 and 86 °C. The spherulites are not space filling in this temperature range as evidenced by circular Vv patterns[32] (Figure 7) and the increase of the spherulite diameter (crossed squares in Figure 6). Clearly, the sharp initial exothermic DSC peak between 95 and 85 °C in Figure 2 delimits the temperature region of spherulite growth, i.e., primary crystallization. In that respect the ESLD is certainly irrelevant because there is no reason why only a specific fraction of the unimodal ESLD would contribute to primary crystallization. The longest ethylene sequences from the ESLD determine the onset of the high-temperature crystallization peak but not its offset. The end point of the spherulite radius increase coincides with the point at which the excess Vv scattering disappears because the radius determined by SALLS is heavily weighted toward larger values. The radius measured at any time corresponds to that of the largest spherulites present in the sample volume. Consequently, the radii of the spherulites that are generated earliest and survive longest before impingement, are probed selectively. The first diameter that could be extracted reads 9 μm at 90 °C. Hv intensity was detected at higher temperatures but these patterns were too weak to be processed.

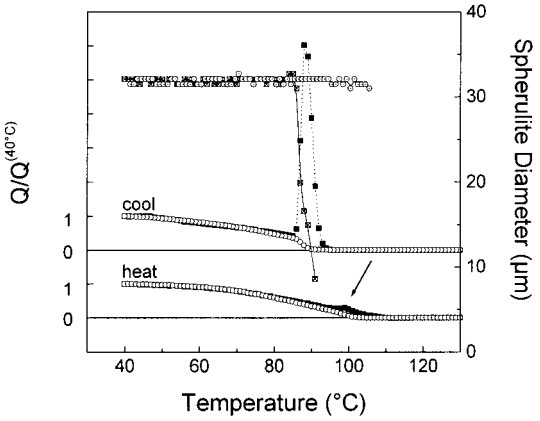

Figure 6. Crossed squares and dotted open circles: the spherulite diameter of JW1120 during cooling and heating at 10 °C/min: open circles, $\{Q_{Hv}\}/\{Q_{Hv}^{(40°C)}\}$; full squares, $\{Q_{Vv}\}/\{Q_{Vv}^{(40°C)}\}$.

During heating $\{Q_{Vv}\}/\{Q_{Vv}^{(40°C)}\}$is also larger than $\{Q_{Hv}\}/\{Q_{Hv}^{(40°C)}\}$at high temperatures (arrow in Figure 6), but the difference is much smaller compared to that in the cooling run. The spherulite diameter, however, at these temperatures does not decrease and the dominating contribution in the Vv patterns has a clear 2-fold symmetry indicating that spherulites are still space filling. The appearance of excess Vv scattering must thus be due to micrometer scale regions with a different mean polarizability (i.e., crystallinity) *inside* the spherulites. Randomly structured and arranged crystallinity inhomogeneities give rise to a circularly symmetrical, exponentially decaying contribution in the Vv-patterns with a scattering power proportional to $\langle\eta^2\rangle$, which for

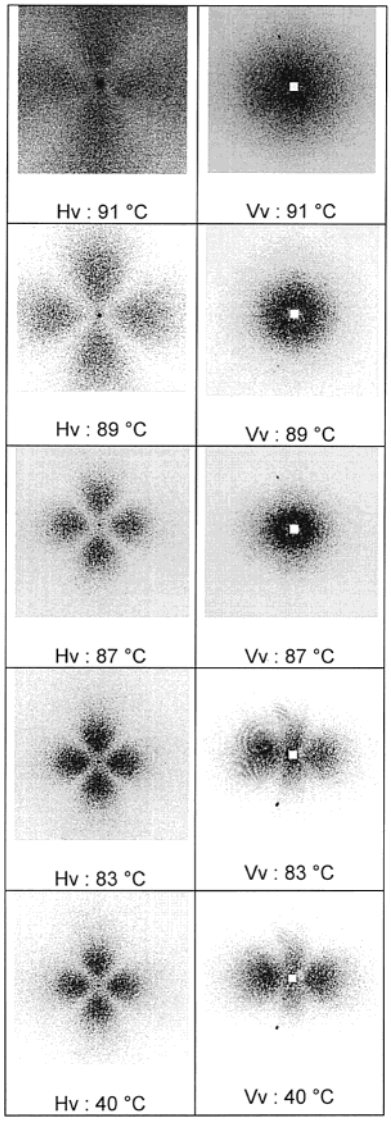

Figure 7. Some representative Hv (left) and Vv (right) patterns collected during cooling at different temperatures. For Hv the polarizers are crossed (diagonal with respect to the images) and for Vv they are parallel (both horizontal with respect to the images).

systems with two different crystallinity fractions can be written as[59]

$$\langle \eta^2 \rangle = \phi_a \phi_b (\alpha_a - \alpha_b)^2 \qquad (30)$$

with ϕ_a and ϕ_b the volume fractions and α_a and α_b the polarizabilities of the fractions inside the spherulites. This equation can be considered as the SALLS equivalent of the third term in eq 9 where the contrast for SAXS is generated by a difference in (electron) density. For X-ray as well as for light scattering, the contrast is actually determined by the difference in internal crystallinity. A small difference in crystallinity between these internal regions may account for the low intensity of the maximum in $\{Q_{Vv}\}/\{Q_{Vv}^{(40°C)}\}$ compared to that of the cooling experiment where the polarizability difference between growing spherulites and the surrounding amorphous matrix is larger.

Figure 8 displays the background corrected SAXS patterns for the cooling run. The weak scattering at low angles points at large scale stack heterogeneity, rather than broad layer and stacking distributions. These data

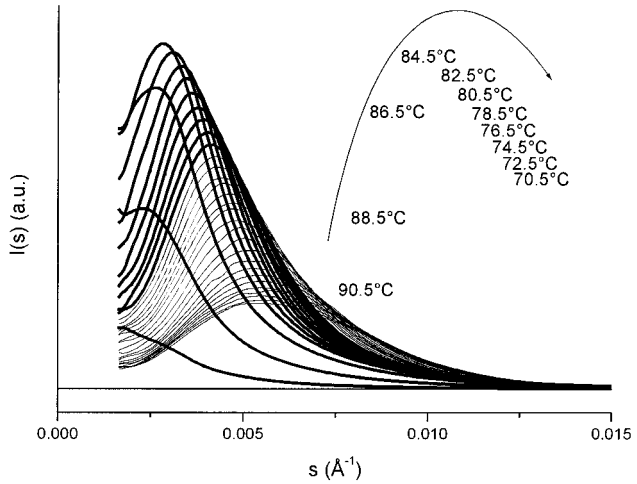

Figure 8. SAXS scattering profiles during cooling after background correction, illustrating the absence of scattering at very low angles. The patterns corresponding to structures with a nonhomogeneous crystallinity distribution are represented with a thick line and the labeled arrow highlights their temperature evolution.

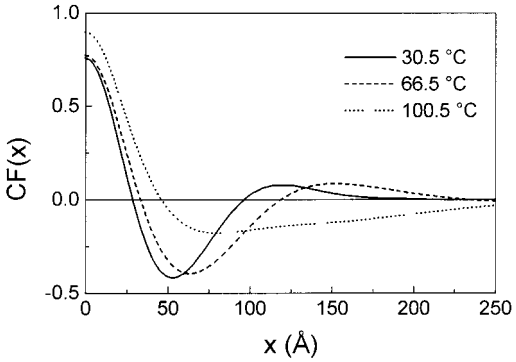

Figure 9. Evolution of some characteristic CF(x) functions at different temperatures during heating.

were processed according to both the A−CA and CA−CA methods. Below a given temperature, however, the morphology is homogeneous and a distinction between the two models is no longer meaningful (i.e., ϕ_1 equals ϕ_2). The experimental SAXS curves that correspond to homogeneous morphologies are represented with a thin line in Figure 8.

All correlation functions tend to zero at large distances, which again is indicative for the absence of zero-order scattering, as illustrated in Figure 9 with some characteristic CF(x) functions of the heating experiment. Correlation functions with a plateau minimum are obtained at high temperatures and allow determination of T_c. These T_c values were used as input during processing according to the CA−CA procedures since—as mentioned in the Experimental Section—no second long period is observed at any temperature.

It is of interest to briefly discuss all combinations of two fractions that in principle are compatible with a given set of Q_c, A, and LP_1 values, irrespective of whether the absence of a second long period is due to a low stacking order in fraction 2 or to the presence of a skew, continuous crystallinity distribution. Values for α_1 were calculated from eq 21 and plotted in Figure 10 as a function of $2/O_{S2}$, using (arbitrarily) the Q_c, A, and LP_1 data of the heating experiment at 90.5 °C. The limits for $2/O_{S2}$ are $A/Q_C \leq 2/O_{S2} \leq \infty$. Figure 10 also displays T_c based on eq 25 together with ϕ_1, ϕ_2, and the

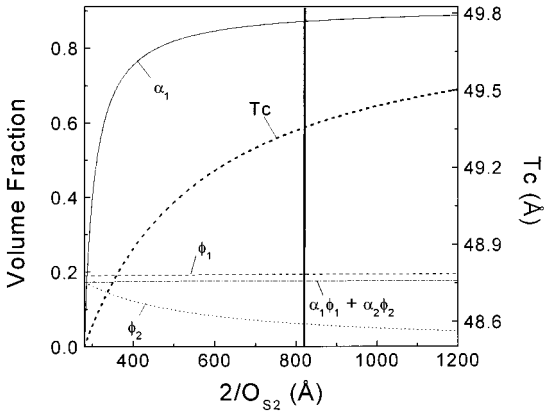

Figure 10. Different possible combinations of T_c, α_1, ϕ_1, ϕ_2, and $\alpha_1\phi_1 + \alpha_2\phi_2$ based on the CA−CA model for the SAXS pattern during heating at 90.5 °C. The lower value for $2/O_{S2}$ is the lower limit. The high-end limit for $2/O_{S2}$ is ∞. The value at the top of the right vertical axis represents the corresponding high-end limit for T_c. The value at the top of the left vertical axis corresponds to the high-end limit of α_1. The thick vertical line crosses the true values for this particular experiment.

overall crystallinity based on eqs 23, 24, and 7, respectively. The parameters calculated with $2/O_{S2}$ equal to ∞ are identical to those obtained with the A−CA model. At the low-end limit $\alpha_1 = 0$ and the crystallinity is expected to be equal to ϕ_2 and homogeneously distributed over the entire volume. However, ϕ_2 differs from ϕ_1, highlighting an incompatibility and thus leading to the conclusion that the crystallinity *cannot* be distributed homogeneously. Similarly, at this limiting point $2/O_{S2}$, which can be considered as the (virtual) long period associated with fraction 2, equals 281 Å and is different from the experimental value of the long period (256 Å). It can be stated that the crystallinity is not homogeneously distributed over the volume whenever A/Q_c differs from the experimental long period. The true values for the parameters in Figure 10 are at the position of the thick vertical line, which intersects the T_c value obtained from the plateau minimum in $K(x)$. The solution critically depends on the accuracy of T_c, which has to be better than 1 Å in the present example. Hence, error estimates like those introduced in the Experimental Section are important. Finally, Figure 10 also illustrates that the choice of T_c or $2/O_{S2}$ has little effect on ϕ_1 and the overall crystallinity. For these parameters the A−CA and CA−CA procedures yield comparable results.

The SAXS CA−CA based overall (volume) fraction crystallinities in Figure 11 agree with the DSC (mass) fraction crystallinities in Figure 2. Note in particular the steeper crystallinity increase at 50 °C during cooling. Error bars are added to the cooling data and are only significant above $\Phi = 0.3$. This is due to the characteristics of eq 16, which yields a large variation in ϕ for a small variation in $\phi(1 - \phi)$ for ϕ close to 0.5. The CA−CA data do not significantly differ from those obtained by using the A−CA procedure.

Figures 12 and 13 focus on the high-temperature windows during cooling and heating, respectively, and give all CA−CA- and A−CA-based volume fractions. The crystallinity below 70.5 °C during cooling and below 86.5 °C during heating can be considered as homogeneously distributed since ϕ_1 equals ϕ_2 within experimental error. The other extreme is touched at high temperatures, i.e., the A−CA limiting values are obtained with $\phi_2 = 0$ and $\alpha_1 = \alpha_S$. At intermediate temperatures a split of the

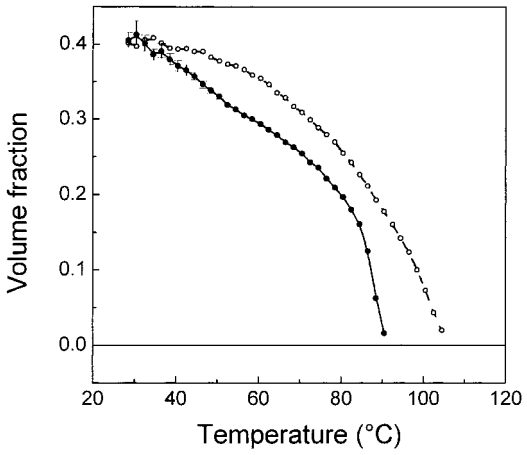

Figure 11. SAXS overall volume fraction crystallinities based on the CA−CA approach during cooling (full circles) and heating (open circles). Error bars are added to the cooling data.

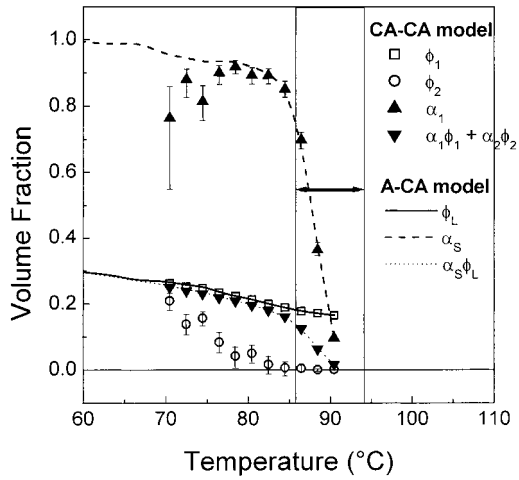

Figure 12. Comparison of characteristic volume fractions during cooling, according to the A−CA and CA−CA approach, respectively. The double headed arrow marks out the temperature range in which excess Vv light scattering is observed.

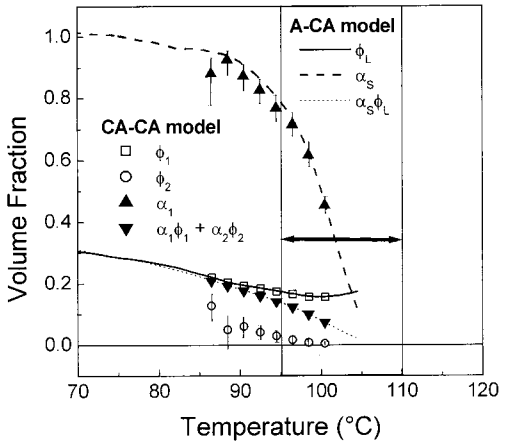

Figure 13. Comparison of characteristic volume fractions during heating, according to the A−CA and CA−CA approach, respectively. The double headed arrow marks out the temperature range in which excess Vv light scattering is observed.

structure into two fractions with a different nonzero crystallinity makes sense.

The evolution of the volume fractions in Figure 12 suggest a morphology development with decreasing temperature according to the sequence of structures

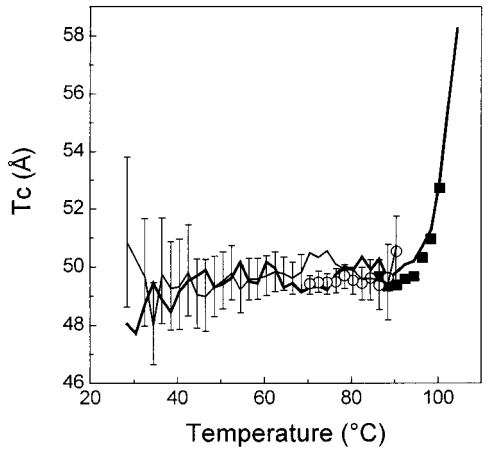

Figure 14. T_c according to the A−CA model during cooling (thin line) and heating (thick line). The results based on the CA−CA model are represented by open circles and full squares, respectively. Error bars are added to the CA−CA-based cooling data and to the A−CA cooling data at temperatures where the crystallinity distribution is homogeneous.

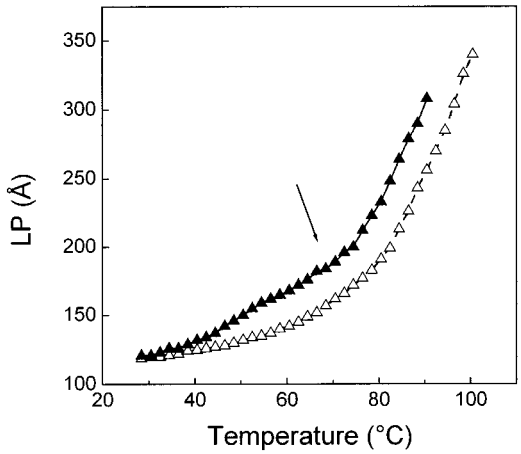

Figure 15. LP during cooling (full symbols) and heating (open symbols). The arrow points to a discontinuity in the evolution of LP during cooling.

2−3−3′−4−5 introduced in Figure 1. An initial stage involving isolated lamellae is not observed. The SALLS-based temperature range associated with primary crystallization is indicated with a double-headed arrow and connects structure 2 at the high-temperature side with structure 3 at the lowest temperature. The steep increase of α_1 accounts for the rapid overall crystallinity increase in this temperature range and is linked to primary crystallization, i.e., spherulite growth and the nucleation of new spherulites. At spherulite impingement roughly 10% of the spherulite internal volume seems to have remained fully amorphous ($\alpha_2 = 10\%$ and $\phi_2 = 0$ at 86 °C). The crystallinity in this fraction 2 increases quite rapidly during further cooling (giving rise to a subsequent series of structure-3′-like overall morphologies) to reach at 70 °C the same crystallinity as in fraction 1. At this temperature the structure is homogeneous like in step 4 of Figure 1. The decrease of α_1 is plausible at the changeover to a homogeneous crystallinity situation because the crystallinities in the fractions become comparable. At this stage, fraction boundaries become diffuse and may shift. Finally, the crystallinity increases further by lamellar insertion only, and leads to structure 5. Indeed, all increases of ϕ_1 and ϕ_2 are due to the insertion of new lamellae and not to lamellar thickening since T_c remains constant within experimental error during the entire crystallization process as depicted in Figure 14. Lamellar insertion is directly reflected in a decrease of the long period, LP, concomitant to the increase of ϕ_1 as illustrated in Figure 15.

There is a rather sharp inflection point in the evolution of LP (see arrow in Figure 15) at 70 °C, which is the temperature associated with the transition to a homogeneous crystallinity distribution. This correlation points to a continuous but skew crystallinity distribution with the most probable crystallinity (artificially) put in fraction 1, i.e., ϕ_1, rather than to a true bimodal distribution. Remember that such systems are split into a—from a descriptive point of view—best set of two fractions with a different crystallinity. All data are compatible with the existence of negatively skewed crystallinity or a positively skewed LP distribution at spherulite impingement. This LP distribution becomes more symmetric while shifting to lower values with decreasing temperature, i.e., the high-end tail shifts faster than the peak of the distribution. The faster shift of the high-end tail is deduced from the faster increase of ϕ_2 compared to that of ϕ_1. Concomitantly, as the distribution becomes more symmetric, the most probable LP value transforms into a true number-average value. At this stage all local long periods have evolved to a comparable—e.g., characteristic—value below which further lamellar insertion is not favored since the rate of LP reduction below that temperature is clearly lower than above it. The existence of a characteristic intercrystallite distance below which the insertion of new lamellae becomes impossible at a given temperature was suggested first by Strobl et al. in the case of a low-density PE.[60,61] Crystallization is prevented by an enrichment of the amorphous intercrystallite layer with noncrystallizable units (hexyl branches in the present case) but is possible at lower temperatures and occurs first in the thickest amorphous layers where the concentration of comonomer units is the lowest. This preference for lamellar insertion in the thicker amorphous layers may account for the more rapid decrease of the LP high-end tail (increase of ϕ_2) compared to that of the smaller most probable value (increase of ϕ_1) in the temperature range 86.5−70 °C. Strobl further argues that such crystals do not need a separate nucleation and visualizes them as crystals that progressively grow thinner with decreasing temperature in the confinement between inclined neighboring crystals.[61] In our opinion, however, the opposite is true for at least a small fraction of the inserted secondary lamellae around 50 °C. At that temperature, the crystallization rate (decrease of LP) suddenly accelerates like the DSC crystallinity. This discontinuity is incompatible with the continuous process suggested by Strobl. A homogeneous type of nucleation is quite likely since the probability of having heterogeneous nuclei with activity at that specific temperature, is very low. Whether "pinning" or pronounced "overcrowding" due to the comonomer enrichment is the underlying reason for this crystallization with postponed nucleation cannot be decided from the present data.[7] In any case, these crystals are very small or have many defects because they do not contribute significantly to the orthorhombic 110 WAXD crystallinity index. There are no indications in the WAXD patterns for other crystal lattice types such as, e.g., hexagonal, which would obviously also not contribute to the orthorhombic 110 index. A small and sharp

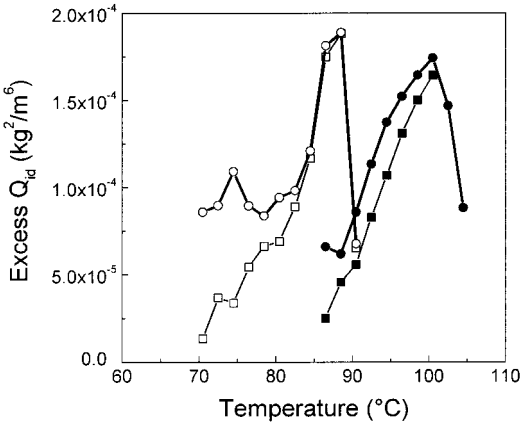

Figure 16. Excess Q_{id} (third term of eq 9), based on the CA−CA model (squares) and the A−CA model (circles) during cooling (open symbols) and heating (full symbols).

endothermic peak like the one around 50 °C in Figure 2 is quite often observed some 30 °C below the high-temperature crystallization peak in the case of homogeneous copolymers with relatively low comonomer content.[10,11] This peak is different from the broad low-temperature crystallization peak mentioned in the Introduction, which is characteristic for samples with a relatively high comonomer content.

Figure 13 illustrates how during subsequent heating the sequence of structures is met again in reversed order, 5−4−3′−3−2, with changeover temperatures that are slightly shifted toward higher temperatures. The decrease of the crystallinity below 86.5 °C, which is best evaluated from Figure 11, is fully due to the melting of secondary inserted lamellae. A stepwise lowering that would correspond to the stepwise increase during cooling around 50 °C is not observed. The changes of LP (Figure 15) and of the crystallinity estimates below 40 °C (Figure 11) nearly overlap with those of the cooling run and are indicative for reversible crystallization and melting as described by Alizadeh et al.[7] in the case of imperfect crystals grown at low temperatures. The structure is no longer homogeneous (i.e., the crystallinity distribution becomes skew) above 86.5 °C. Above 95.5 °C, truly amorphous areas are developed since ϕ_2 equals zero. In this temperature range, there is excess Vv light scattering. Note that a CA−CA analysis could not be performed at the two highest temperatures because no accurate values for LP are available.

Because of the availability of α_1, α_2, ϕ_1, and ϕ_2 one can calculate the zero-order contribution to Q_{id}, which is assumed not to contribute to the observed scattering patterns, using the third term in eq 9. This is of interest since it highlights apparent incompatibilities with the SALLS data of Figure 6. As mentioned above, this third term is the SAXS equivalent of eq 30 for SALLS. The results are represented in Figure 16 together with the excess Q_{id} corresponding to the A−CA model, based on α and ϕ_L.

The cooling and heating data both display a maximum as do the SALLS Vv excess contributions but the maximum in the excess Q_{id} of the cooling experiment is hardly higher than that of the heating experiment in contrast to the SALLS data. Second, SAXS excess is observable down to lower temperatures compared to SALLS. Finally, the SAXS contrast during cooling is *identical* to that during heating in the temperature ranges where SALLS excess occurs, and equal to the electron density difference between amorphous material and a semicrystalline fraction. This observation conflicts with the idea of having a smaller SALLS contrast and thus a smaller crystallinity difference between the fractions inside the melting spherulites as compared to the crystallinity difference between growing spherulites and the surrounding amorphous matrix.

All discrepancies can be accounted for by considering size effects. There is no contribution to the excess Vv scattering from heterogeneities that are smaller than approximately one μm, accounting for the absence of excess Vv scattering at low temperatures. Very little excess Vv scattering is observed if only a small fraction of the phases detected by SAXS reaches the required dimensions, as could be the case at high temperatures during melting. During spherulite growth in the cooling experiment, the phases are sufficiently large, and the excess Vv scattering is very pronounced.

The weak excess Vv SALLS during melting can also be explained in an alternative way. Some of the small semicrystalline regions, together with some of the neighboring amorphous regions, can form micrometer-scale domains with an intermediate crystallinity. The crystallinity difference between those domains will be small and result in weak excess Vv SALLS scattering. Both scenarios imply heterogeneity on different scales.

Note that the SAXS excess function according to the CA−CA model during cooling decreases slowly toward zero, the value expected for a homogeneous crystallinity distribution. The values based on the A−CA model, remain more or less constant but finally jump to zero below 70 °C. The "more natural" evolution toward zero of the excess Q_{id}, based on the CA−CA model, can be taken as an argument in favor of this model. The same holds for the heating experiment. Note that similar stepwise changes are observed in the α_S values in Figures 12 and 13 at the changeover to a homogeneous morphology. They are artifacts and reflect the changeover from an inappropriate use of the A−CA model where actually no amorphous regions exist to a legitimate use in the limiting case of a homogeneously distributed crystallinity.

Finally, some additional comments should be made on the evolution of T_c. At all temperatures a true overall number-average crystal thickness is computed. At high temperature, the value of $K(x)_{min}$ is used and at lower temperatures—when the crystallinity is homogeneously distributed—eq 16 with LP being a true number-average long period. The T_c values in Figure 14 are smaller than the AFM based estimates. In general, smaller SAXS estimates are also obtained for the long period (inter-crystallite distance) except for the crystals that are most closely packed in the AFM images. The SAXS-based estimates are believed to be more accurate. The AFM overestimations could be due to a slight tilt of the stacks or to the existence of differences between the bulk and surface morphology.

In principle, T_c should decrease during cooling because of an increasing degree of supercooling and thus the growth of progressively thinner crystals. In the present case, however, T_c does not change (Figure 14). This expected crystal thickness evolution disappears if—as soon as crystals are generated at a given temperature—fast thickening occurs to a copolymer (comonomer content) specific limiting value. Crist and Claudio recently discussed the option of having lamellar thickening of copolymer crystals that are grown at relatively

high temperatures.[15] Fast thickening can account for the constancy of T_c in a broad temperature window and in addition justifies the assumption of having an identical T_c value in the fractions 1 and 2 in the CA−CA analysis. The comonomer unit content in the melt of fraction 2 is most likely identical to that of fraction 1 since a large-scale (i.e., "stack scale") segregation according to composition (comonomer content) is very unlikely for homogeneous copolymers that have negligible compositional differences between polymeric chains. On the other hand, there is a relevant change of the composition of the melt at the boarders of the crystals. These layers, however, do not penetrate far into the sample volume.[60,61]

T_c increases suddenly at the end of the melting experiment and exceeds the values obtained during cooling. This behavior is thought to be indicative for melting and recrystallization into thicker crystals.

Conclusions

Using a combination of scattering techniques, AFM and DSC a detailed description of the structural changes that occur during the crystallization and melting of a homogeneous copolymer of ethylene and 5.2 mol % 1-octene has been obtained.

DSC and SALLS point to 94 °C as the onset temperature for crystallization during cooling at 10 °C per min. The initial sharp DSC exothermic peak and the excess Vv-scattering occur in the same temperature range and are associated with the process of primary crystallization. The crystallinity distribution inside the spherulites at impingement is asymmetric with a most probable local crystallinity of 18% and with about 10% of the spherulite internal volume remaining amorphous. Upon further cooling, crystallinity develops more rapidly in the least crystalline regions compared to areas where crystals are more closely packed. As a result, the crystallinity distribution becomes progressively symmetric. The crystallinity is homogeneously distributed over the sample volume at and below 70 °C and further increases slowly by insertion of new crystals. At 50 °C, this process accelerates probably due to the onset of homogeneous nucleation. The crystals involved are either small or very imperfect because they do not contribute to the WAXD crystalline reflections. The average thickness of the crystals remains constant during cooling and heating with, however, a slight increase at the end of the heating run, which is taken as evidence for melting and recrystallization into thicker crystals. The crystals that were formed during previous cooling melt in the reverse sequence of their formation since the evolution of LP as a function of temperature during heating is comparable to that of the cooling experiment, taking hysteresis into account. This hysteresis can also be observed in the evolution of most volume fraction estimates. The only difference occurs at the highest temperatures where the process of primary crystallization is not reversed since spherulites, obviously, do not melt back toward their primary nucleus. Spherulite melting is, however, a very heterogeneous process during which regions with different degrees of crystallinity develop.

The interpretation of the SAXS results relies on an extension of the linear correlation function analysis to two-phase (crystalline−amorphous) layer systems consisting of two fractions with a different crystallinity (CA−CA model). This approach is particularly suited for the characterization of bimodal crystallinity distributions but yields meaningful data also in the case of unimodal, skew distributions. A best agreement of the SAXS-based crystallinity estimate with that of DSC and WAXD was obtained by assuming that the crystalline density in the core of the lamellar crystallites equals that of undistorted linear polyethylene, implying that the interphase between crystalline and amorphous layers is partially DSC and WAXD crystalline.

Acknowledgment. B.G. is indebted to the IWONL and IWT for research grants. H.R. is grateful to FWO-Vlaanderen for continuous support and equipment. B.G. and H.R. thank DSM for continuous interest and sample support. Part of this work was performed in the framework of BIL 99/023. The E.U. is acknowledged for support under the TMR/LSF program to the EMBL Hamburg Outstation, reference number ERBFMGECT980134. M. Basiura and G. de Schaetze (KU Leuven) are acknowledged for assistance with the AFM work.

References and Notes

(1) Vonk, C. G.; Reynaers, H. *Polym. Commun.* **1990**, *31*, 190.
(2) Laupretre, F.; Monnerie, L.; Barthelemy, L.; Vairon, J. P.; Sauzeau, A.; Roussel, D. *Polym. Bull. (Berlin)* **1986**, *15*, 159.
(3) Pérez, E.; VanderHart, D. L.; Crist, B.; Howard, P. R. *Macromolecules* **1987**, *20*, 78.
(4) Pérez, E.; VanderHart, D. L. *J. Polym. Sci., Part B: Polymer Phys.* **1987**, *25*, 1637.
(5) Flory, P. J. *Trans. Faraday Soc.* **1955**, *51*, 848.
(6) Vonk, C. G. *J. Polym. Sci., Part C: Polym. Lett.* **1986**, *24*, 305.
(7) Alizadeh, A.; Richardson, L.; Xu, J.; McCartney, S.; Marand, H.; Cheung, Y. W.; Chum, S. *Macromolecules* **1999**, *32*, 6221.
(8) Bensason, S.; Minick, J.; Moet, A.; Chum, S.; Hiltner, A.; Baer, E. *J. Polym. Sci., Part B: Polym. Phys.* **1996**, *34*, 1301.
(9) Mathot, V. B. F.; Scherrenberg, R. L.; Pijpers, M. F. J.; Engelen, Y. M. T. In *New trends in Polyolefin Science and Technology*; Hosoda, S., Ed.; Research Signpost: Trivandum, India, 1996; p 71.
(10) Mathot, V. B. F. In *Calorimetry and Thermal Analysis of Polymers*; Mathot, V. B. F., Ed.; Hanser Publishers: New York, 1994, Chapter 9, p 231.
(11) Vanden Eynde, S.; Mathot, V.; Koch, M. H. J.; Reynaers, H. *Polymer* **2000**, *41*, 3437.
(12) Androsch, R. *Polymer* **1999**, *40*, 2805.
(13) Androsch, R.; Blackwell, J.; Chvalun, S. N.; Wunderlich, B. *Macromolecules* **1999**, *32*, 3735.
(14) Androsch, R.; Wunderlich, B. *Macromolecules* **2000**, *33*, 9076.
(15) Crist, B.; Claudio, E. S. *Macromolecules* **1999**, *32*, 8945.
(16) Hunter, B. K.; Russell, K. E.; Scammel, M. V.; Thompson, S. L. *J. Polym. Sci., Polym. Chem. Ed.* **1984**, *22*, 1383.
(17) Clas, S.-D.; McFaddin, D. C.; Russell, K. E. *J. Polym. Sci., Part B: Polym. Phys.* **1987**, *25*, 1057.
(18) Clas, S.-D.; McFaddin, D. C.; Russell, K. E.; Scammell-Bullock, M. V. *J. Polym. Sci., Part A: Polym. Chem.* **1987**, *25*, 3105.
(19) Clas, S.-D.; Heyding, R. D.; McFaddin, D. C.; Russell, K. E.; Scammell-Bullock, M. V.; Kelusky, E. C.; St-Cyr, D. *J. Polym. Sci., Part B: Polym. Phys.* **1988**, *26*, 1271.
(20) Mathot, V. B. F.; Scherrenberg, R. L.; Pijpers, T. F. J. *Polymer* **1998**, *39*, 4541.
(21) Peeters, M.; Goderis, B.; Vonk, C.; Reynaers, H.; Mathot, V. *J. Polym. Sci., Part B: Polym. Phys.* **1997**, *35*, 2689.
(22) Peeters, M.; Goderis, B.; Reynaers, H.; Mathot, V. *J. Polym. Sci., Part B: Polym. Phys.* **1999**, *37*, 83.
(23) Goderis, B.; Peeters, M.; Mathot, V. B. F.; Koch, M. H. J.; Bras, W.; Ryan, A. J.; Reynaers, H. *J. Polym. Sci., Part B: Polym. Phys.* **2000**, *38*, 1975.
(24) Goderis, B.; Mathot, V. B. F.; Reynaers, H. *Preprints of Papers*; ACS 218th National Meeting of the American Chemical Society, New Orleans, LA, August 22−26, 1999; American Chemical Society: Washington DC, 1999; Semicrystalline polymers, p 344.
(25) Zachmann, H. G. *Nucl. Instrum. Methods Phys. Res.* **1995**, *B 97*, 209.

(26) Mathot, V. B. F.; Pijpers, M. F. J. *J. Therm. Anal.* **1983**, *28*, 349.
(27) Mathot, V. B. F. In *Calorimetry and Thermal Analysis of Polymers*; Mathot, V. B. F., Ed.; Hanser Publishers: New York, 1994, Chapter 5, p 105.
(28) Tabar, R. J.; Stein, R. S.; Long, M. B. *J. Polym. Sci.: Phys. Ed.* **1982**, *20*, 2041.
(29) Goderis, B.; Reynaers, H.; Koch, M. H. J.; Mathot, V. B. F. *J. Polym. Sci., Part B: Polym. Phys.* **1999**, *37*, 1715.
(30) Prud'homme, R. E.; Bourland, L.; Natarajan, R. T.; Stein, R. S *J. Polym. Sci.: Polym. Phys. Ed.* **1971**, *12*, 1955.
(31) Tabar, R. J.; Leite-James, P.; Stein, R. S. *J. Polym. Sci.: Polym. Phys. Ed.* **1985**, *23*, 2085.
(32) Stein, R. S.; Rhodes, M. B. *J. Appl. Phys.* **1960**, *31*, 1873.
(33) Yoon, D. Y.; Stein, R. S. *J. Polym. Sci.: Polym. Phys. Ed.* **1974**, *12*, 735.
(34) Akpalu, Y.; Kielhorn, L.; Hsiao, B. S.; Stein, R. S.; Russell, T. P.; van Egmond, J.; Muthukumar, M. *Macromolecules* **1999**, *32*, 765.
(35) Magonov, S. *Polym. Mater. Sci. Eng.* **1998**, *78*, 106.
(36) Bar, G.; Thomann, Y.; Brandsch, R.; Cantow, H.-J. *Langmuir* **1997**, *13*, 3807.
(37) Koch, M. H. J.; Bordas, J. *Nucl. Instrum. Methods* **1983**, *208*, 435.
(38) Boulin, C. J.; Kempf, R.; Gabriel, A.; Koch, M. H. J. *Nucl. Instrum. Methods* **1988**, *A269*, 312.
(39) Rapp, G.; Gabriel, A.; Dosière, M.; Koch, M. H. J. *Nucl. Instrum. Methods* **1995**, *A357*, 178 1995.
(40) Goderis, B.; Reynaers, H.; Scherrenberg, R.; Mathot, V. B. F.; Koch, M. H. J. *Macromolecules* **2001**, *34*, 1779.
(41) Koberstein, J. T.; Morra, B.; Stein, R. S. *J. Appl. Crystallogr.* **1985**, *13*, 2517.
(42) Porod, G. *Kolloid-Z* **1951**, *124* (2), 83.
(43) Strobl, G. R.; Schneider, M. *J. Polym. Sci.: Polym. Phys. Ed.* **1980**, *18*, 1343.
(44) Vonk, C. G. *J. Appl. Crystallogr.* **1973**, *6*, 81.
(45) Afifi, A. A.; Azen, S. P. *Statistical Analysis, A computer Oriented Approach*; Academic Press: New York and London, 1972; pp 91−97.
(46) Debye, P.; Anderson, H. R.; Brumberger, H. *J. Appl. Phys.* **1957**, *28*, 679.
(47) Blundell, D. J. *Polymer* **1978**, *19*, 1258.
(48) Crist, B. *J. Macromol. Sci. Phys.* **2000**, *B39(4)*, 493.
(49) Swan, P. R. *J. Polym. Sci.* **1960**, *42*, 525.
(50) Strobl G. R.; Müller, N. *J. Polym. Sci., Polym. Phys. Ed.* **1973**, *11*, 1219.
(51) Lee, Y. D.; Phillips, P. J.; Lin, J. S. *J. Polym. Sci., Part B: Polym. Phys.* **1991**, *29*, 1235.
(52) Balta-Calleja, F. J.; Vonk, C. in *X-ray Scattering of Polymers*; Elsevier: Amsterdam, 1989.
(53) Vonk, C. G.; Kortleve, G *Kolloid Z. Z. Polym.* **1967**, *220*, 19.
(54) Vonk, C. G.; Pijpers, A. P. *J. Polym. Sci., Polym. Phys. Ed.* **1985**, *23*, 2517.
(55) Ruland, W. *Colloid Polym. Sci.* **1977**, *255*, 417.
(56) Vand, V.; de Boer, J. H. *Proc. K. Ned. Akad. Wet.* **1947**, *50*, 991.
(57) Davis, G. T.; Weeks, J. J.; Martin, G. M.; Eby, R. K. *J. Appl. Phys.* **1974**, *45*, 4175.
(58) Mandelkern, L. *Chemtracts: Macromol. Chem.* **1992**, *3*, 347.
(59) Lee, C. H.; Saito, H.; Inoue, T. *Macromolecules* **1993**, *26*, 6566.
(60) Strobl, G. R.; Schneider, M. J.; Voigt-Martin, I. G. *J. Polym. Sci.: Polym. Phys. Ed.* **1980**, *18*, 1361.
(61) Strobl, G. *The Physics of Polymers, Concepts to understand their Structure and Behavior*; Springer-Verlag: Berlin and Heidelberg, Germany, 1996; pp 181−185.

MA011749C